

Engineering the Low Coordinated Pt Single Atom to Achieve the Superior Electrocatalytic Performance toward Oxygen Reduction

Zhongxin Song, Ya-Nan Zhu, Hanshuo Liu, Mohammad Norouzi Banis, Lei Zhang, Junjie Li, Kieran Doyle-Davis, Ruying Li, Tsun-Kong Sham, Lijun Yang, Alan Young, Gianluigi A. Botton,* Li-Min Liu,* and Xueliang Sun*

Configuring metal single-atom catalysts (SACs) with high electrocatalytic activity and stability is one efficient strategy in achieving the cost-competitive catalyst for fuel cells' applications. Herein, the atomic layer deposition (ALD) strategy for synthesis of Pt SACs on the metal–organic framework (MOF)-derived N-doped carbon (NC) is proposed. Through adjusting the ALD exposure time of the Pt precursor, the size-controlled Pt catalysts, from Pt single atoms to subclusters and nanoparticles, are prepared on MOF-NC support. X-ray absorption fine structure spectra determine the increased electron vacancy in Pt SACs and indicate the Pt–N coordination in the as-prepared Pt SACs. Benefiting from the low-coordination environment and anchoring interaction between Pt atoms and nitrogen-doping sites from MOF-NC support, the Pt SACs deliver an enhanced activity and stability with 6.5 times higher mass activity than that of Pt nanoparticle catalysts in boosting the oxygen reduction reaction (ORR). Density functional theory calculations indicate that Pt single atoms prefer to be anchored by the pyridinic N-doped carbon sites. Importantly, it is revealed that the electronic structure of Pt SAs can be adjusted by adsorption of hydroxyl and oxygen, which greatly lowers free energy change for the rate-determining step and enhances the activity of Pt SACs toward the ORR.

1. Introduction

Polymer electrolyte membrane fuel cells (PEMFCs) are one of the most promising power sources for transportation and portable applications due to their high efficiency, room-temperature operation, and zero greenhouse gas emissions.^[1] However, one of the major challenges for the widespread application of PEMFCs is developing cost-competitive electrocatalysts for cathodic oxygen reduction reaction (ORR). Noble metals, especially platinum (Pt) or Pt-alloy nanoparticles (NPs) are the state-of-the-art heterogeneous catalysts to facilitate the ORR in PEMFCs.^[2] As the active Pt atoms are only located on the NPs' surface, the Pt atom utilization in the NPs-based electrocatalysts is low and the internal Pt atoms cannot exhibit their activity.^[3] Therefore, research to maximize the atom utilization efficiency and decrease the Pt loading has been considered to be the primary task in

Dr. Z. Song
Shenzhen Key Laboratory of Polymer Science and Technology
Guangdong Research Center for Interfacial Engineering of Functional Materials
College of Materials Science and Engineering
Shenzhen University
Shenzhen 518060, China

Dr. Z. Song, Dr. M. N. Banis, Dr. L. Zhang, J. Li, K. Doyle-Davis, R. Li, Prof. X. Sun
Department of Mechanical and Materials Engineering
University of Western Ontario
London, Ontario N6A 5B9, Canada
E-mail: xsun@eng.uwo.ca

Dr. Y.-N. Zhu, Prof. L.-M. Liu
Beijing Computational Science Research Center
Beijing 100193, China
E-mail: liminliu@buaa.edu.cn

 The ORCID identification number(s) for the author(s) of this article can be found under <https://doi.org/10.1002/smll.202003096>.

Dr. Y.-N. Zhu, Prof. L.-M. Liu
School of Physics
Beihang University
Beijing 100083, China

Dr. H. Liu, Prof. G. A. Botton
Department of Materials Science and Engineering
McMaster University
Hamilton, Ontario L8S 4L8, Canada
E-mail: gbotton@mcmaster.ca

Prof. T.-K. Sham
Department of Chemistry
University of Western Ontario
London, Ontario N6A 5B7, Canada

Dr. L. Yang, A. Young
Ballard Power Systems Inc.
Burnaby, British Columbia V5J 5J8, Canada

DOI: 10.1002/smll.202003096

achieving low-cost electrocatalysis for PEMFCs. Downsizing metal NPs to clusters in sub-nanometer or even single atoms (SAs) has the powerful ability to enhance the metal atom utilization.^[4] Unlike conventional NP catalysts, single-atom catalysts (SACs) display characteristics like low-coordination configuration, quantum size effect, strong SA–support interaction, which induce the unsaturated coordination environment of the active centers in SACs and play a significant role in improving the catalytic activity and stability.^[4b,5] In 2011, Zhang and co-workers employed a co-precipitation method to prepare Pt SACs supported on iron oxide, which show high activity and stability for CO oxidation.^[6] Sun et al. reported the fabrication of Pt SACs on graphene by atomic layer deposition (ALD), the as-prepared ALD Pt SACs showed ten times higher activity for methanol oxidation and superior CO tolerance compared to the state-of-the-art Pt/C catalyst.^[7] In addition, the mass activity of Pt SACs on nitrogen-doped graphene is ≈ 374 times greater than that of the Pt/C catalyst for the hydrogen evolution reaction.^[8]

To now, great strides have been made in the field of SACs' synthesis, characterizations, and the preliminary applications.^[9] However, there remains tough challenges such as poor stability and low atoms density that hinder SACs' widespread application. Owing to the high specific energy of isolated atoms, most available SACs must keep a low loading (usually near 0.1 wt%) to avoid aggregation, which limits the development of SACs.^[10] To achieve SACs with high activity and stability, developing a strategy that can prepare the high density of isolated single atoms with strong metal atom–support interactions is considered as an effective strategy.^[9e,11] Metal–organic frameworks (MOFs) with high surface area and fine tunable crystalline structure have attracted increasingly attentions in fabricating the SACs and/or catalyst support.^[12] Herein, for the first time, the Pt SACs were prepared on the MOF-derived N-doped carbon (MOF-NC) support by an ALD technique. To achieve the high Pt SA loading, the MOF-NC with high surface area and abundant nitrogen-doping sites is selected as the support for anchoring Pt SAs. Owing to rich concentration of nitrogen-doping sites, the MOF-NC support is expected to form a strong covalent bonding with Pt SAs, thereby resulting in a strong Pt SA–support interaction, which contributes to the enhanced stability of Pt SACs. Compared with Pt NPs, the as-prepared Pt SA catalyst shows much enhanced mass activity (6.5 times) and good stability in electrocatalysis of the ORR, with generation of H₂O product in acid electrolyte. Density functional theory (DFT) calculations indicated the four-electron ORR pathway on Pt SACs, which identified the origin active sites of Pt SAs in boosting the ORR and revealed the mechanism for the improved activity of Pt SAs in comparison with Pt NP catalysts.

2. Results and Discussion

The synthesis protocol starts from the MOFs (ZIF-8) precursor by a wet chemical method (Supporting Information). The Zn-based ZIF-8 precursors are carbonized at 1000 °C in Ar atmosphere to achieve the nitrogen-doped nanocarbon of ZIF-NC. Serving as the support material, ZIF-NC is put into a vacuum chamber, and the ALD process is applied to deposit the

Pt catalyst on ZIF-NC support. By adjusting the Pt precursor deposition time of 30 s, 1.0 min, and 5.0 min during ALD synthesis, the precisely size-controlled Pt SAs, Pt subclusters (Pt SCs), and Pt NPs are fabricated on the ZIF-NC support, respectively (experimental details are shown in the Supporting Information). Physical characteristics of the as-prepared ZIF-8 precursor and ZIF-NC support are performed prior to ALD of Pt. The scanning electron microscopy (SEM) image (Figure S1a, Supporting Information) and X-ray diffraction (XRD) patterns (Figure S1b, Supporting Information) show that ZIF-8 polyhedrons with the crystal structure and the average particle size of 80 nm are prepared. After high-temperature carbonization, the ZIF-8 crystals are transformed into the nitrogen-doped nanocarbons named as ZIF-NC. The SEM image in Figure S1c (Supporting Information) shows that ZIF-NC well maintained the polyhedron morphology from the parent ZIF-8, and the particle size exhibits no change compared with the ZIF-8 precursor. The XRD patterns performed on the sample of ZIF-NC (Figure S1d, Supporting Information) indicate the characteristic carbon structure of ZIF-NC, suggesting the high degree of graphitization and electronic conductivity is achieved for the ZIF-NC. The X-ray photoelectron spectroscopy (XPS) (Figure S2, Supporting Information) determines that the main components of ZIF-NC are carbon (92.3 at%) with 5.1 at% of nitrogen dopants. The N-doping sites in the carbon network of ZIF-NC support are expected to benefit in anchoring the ALDPt atoms and favor in boosting the catalytic activity and stability.

To confirm the microstructure and distribution of ALDPt on ZIF-NC support, high-angle-annular dark field–scanning transmission electron microscopy (HAADF–STEM) is used to distinguish the Pt SAs, Pt SCs, and Pt NPs. **Figure 1** shows the HAADF–STEM images of the as-prepared Pt SAs–ZIF-NC, Pt SCs–ZIF-NC, Pt NPs–ZIF-NC, which are obtained by ALD dosing Pt precursor on ZIF-NC support for 30 s, 1.0 min, and 5.0 min, respectively. It is known that the contrast of HAADF–STEM image is proportional to the atomic number of the elements in the sample; the heavier Pt atoms thus display brighter intensity compared to the lighter carbon/nitrogen atoms in the support. As shown in Figure 1a, the ZIF-NC maintained their original morphology after 30 s ALD of Pt. Further enhancing the magnification (Figure 1b), small bright dots corresponding to Pt can be observed with uniform distribution on the ZIF-NC support. The atomic-resolution HAADF-STEM image in Figure 1c clearly identifies the presence of individual bright dots (marked in the white circles), which are considered as the isolated Pt atoms dispersing on the surface of ZIF-NC support. The loading amount of Pt SAs on ZIF-NC is 0.8 wt% according to the inductively coupled plasma optical emission spectrometer (ICP-OES) analysis. For the sample of ALDPt–ZIF-NC prepared with 1.0 min dosing of Pt precursor as shown in Figure 1d,e, the Pt species with a high density are uniformly dispersed on the ZIF-NC support. The HAADF-STEM image in Figure 1f displays that most Pt species are formed as the subclusters with the average size of 0.85 nm (marked in the white square); only small proportion of Pt species are in form of isolated single atoms and no obvious Pt crystalline particle is detected. It confirms that Pt SCs are successfully prepared on ZIF-NC support by 1.0 min ALD dosing of the Pt precursor. Further increasing ALD pulse

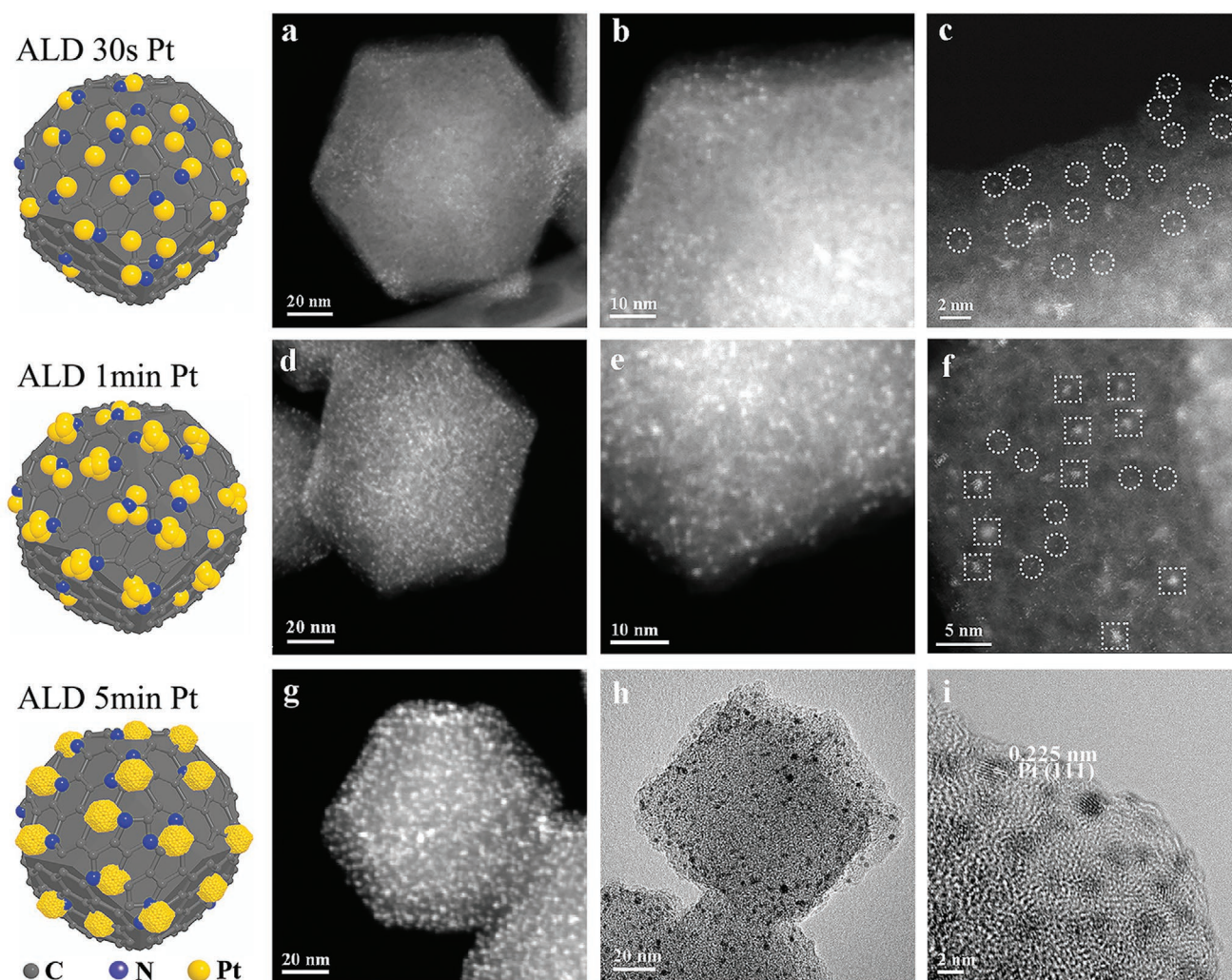


Figure 1. HADDF-STEM images for samples of a–c) Pt SAs-ZIF-NC prepared with 30 s ALD (isolated Pt single atoms marked in the circle), d–f) Pt SCs-ZIF-NC prepared with 1.0 min ALD (Pt subclusters marked in the square and Pt single atoms marked in the circle), and g–i) Pt NPs-ZIF-NC prepared with 5.0 min ALD of exposure MeCpPtMe₃ precursor.

time of Pt precursor to 5.0 min, a high Pt density and crystalline Pt NPs with an average size of 2 nm can be obtained on the ZIF-NC support (Figure 1g–i). The HAADF-STEM results provide evidence for the successful preparation of highly distributed Pt SAs, Pt SCs, and Pt NPs on the N-doped ZIF-NC substrate, corresponding 0.8, 1.5, and 10.5 wt% Pt loading (determined by ICP-OES) can be obtained, respectively, by adjusting the ALD synthesis.

The composition and chemical states of as-prepared ALD Pt SAs, Pt SCs, and Pt NPs on ZIF-NC support are examined by XPS spectra. Pt 4f XPS spectra can be deconvoluted into two sets of peaks for Pt 4f_{7/2} and Pt 4f_{5/2} as shown in **Figure 2a**. Binding energies of Pt 4f doublets centered at 72.8 and 76.0 eV for Pt SAs, which are attributed to the species of Pt(II), indicating Pt atoms are partially oxidized in Pt SAs-ZIF-NC and Pt SCs-ZIF-NC samples. In case of Pt NPs-ZIF-NC, both doublets of 72.8 and 76.0 eV for Pt(II), and lower binding energies of 71.6 and 74.9 eV assigned to metallic Pt(0) are detected. XPS analysis shows that the predominant

doublets at the binding energies of 71.6 and 74.9 eV are ascribed to metallic Pt(0) in the Pt NPs-ZIF-NC. The higher binding energy of Pt SAs than that of Pt NPs indicates the partial oxidation state and lower electron density of Pt atoms in Pt SAs-ZIF-NC. Additionally, the fitted XPS peaks for N 1s of as-prepared ALDPt-ZIF-NC can be deconvoluted into four different bands at ≈398.6, 400.3, 401.1, and 403.0 eV, which correspond to pyridinic N, pyrrolic N, graphitic N, and oxidized N, respectively. Accordingly, the XPS results indicate that the organic linkers in ZIF-8 are transformed into nitrogen-doped carbon. The oxidation state of Pt in Pt SAs-ZIF-NC implies the electron transfer between Pt SAs and the ZIF-NC supporting, suggesting the interaction and anchoring effect of N-dopants to the Pt SAs.

To understand the difference of coordination path, local electronic structure, and the chemical environment between the Pt SAs, SCs to NPs throughout the whole ALDPt-ZIF-NC samples, X-ray diffraction, normalized X-ray near edge spectra (XANES), and the extended X-ray fine structure (EXAFS) spectra at Pt

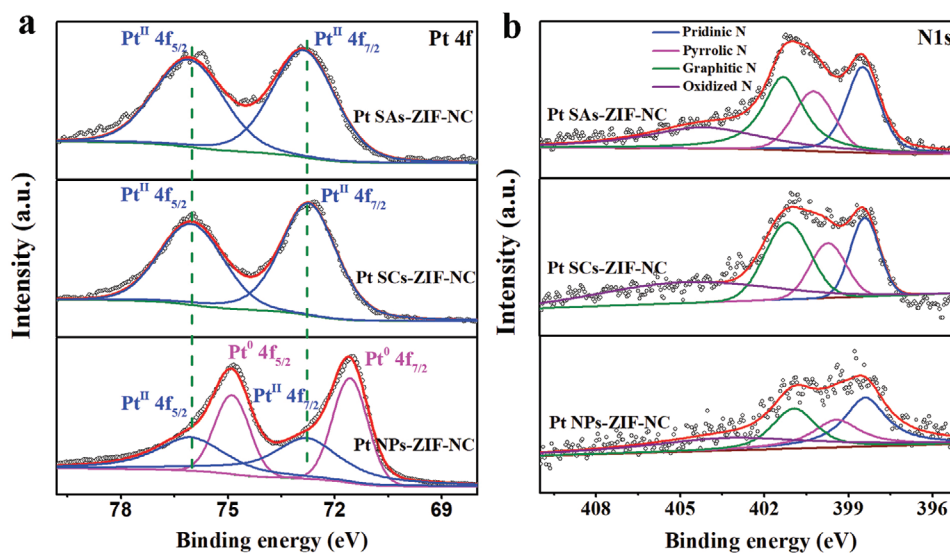


Figure 2. XPS spectrum of Pt SAs-ZIF-NC, Pt SCs-ZIF-NC, and Pt NPs-ZIF-NC for the a) Pt 4f and b) N 1s.

L-edge are studied. XRD patterns in **Figure 3a** show that the MOF-derived ZIF-NC support has a wide characteristic peak of graphite (002) at 26° , indicating a carbon nature of ZIF-NC.

After ALD of Pt SAs and SCs on ZIF-NC support, the XRD patterns of Pt SAs-ZIF-NC and Pt SCs-ZIF-NC do not show any Pt-containing crystal phases, primarily because Pt species are

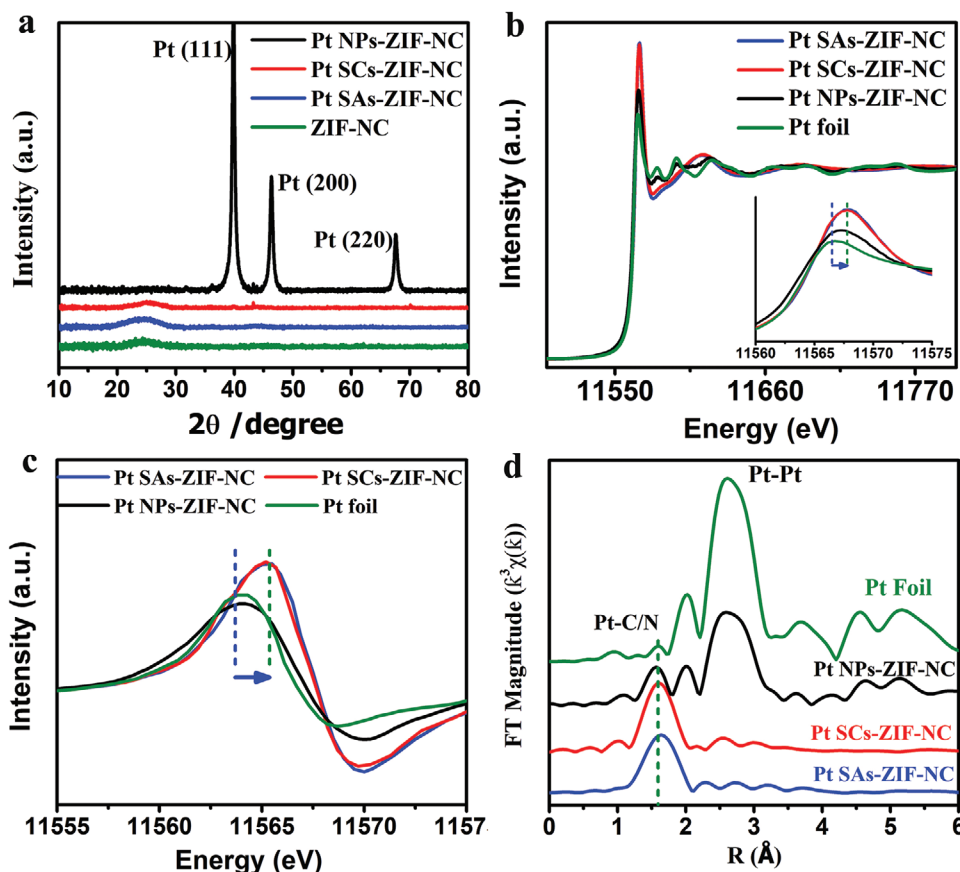


Figure 3. a) The X-ray diffraction patterns of Pt SAs-ZIF-NC, Pt SCs-ZIF-NC, Pt NPs-ZIF-NC, and ZIF-NC. b) The normalized XAFS spectra (XANES and EXAFS) of Pt SAs-ZIF-NC, Pt SCs-ZIF-NC, Pt NPs-ZIF-NC, and Pt foil. c) The normalized derivative spectra at L_3 -edge of Pt SAs-ZIF-NC, Pt SCs-ZIF-NC, Pt NPs-ZIF-NC, and Pt foil. d) The K_3 -weighted Fourier transform spectra of EXAFS at the L_3 -edge of Pt SAs-ZIF-NC, Pt SCs-ZIF-NC, Pt NPs-ZIF-NC, and Pt foil.

presented as the isolated single atoms and isolated subclusters on ZIF-NC, which is consistent with that of the HAADF-STEM analysis. By contrast, with 5.0 min deposition of Pt on ZIF-NC support, the diffraction peaks at 39.8°, 46.2°, 67.6°, and 81.4° corresponding to Pt crystal facets of the face-centered-cubic (fcc) metallic Pt are observed in the as-prepared Pt NPs-ZIF-NC, which is due to the formation of Pt nanocrystals, and the HAADF-STEM image indicates the average Pt particle size is ≈2 nm.

Figure 3b presents the XANES and EXAFS spectra at Pt L₃-edge for the fresh samples of Pt SAs-ZIF-NC, Pt SCs-ZIF-NC, Pt NPs-ZIF-NC, alongside the metallic Pt foil as reference. It should be noted that the white line (WL) peak intensity obtained from the XANES spectra is directly related to the unoccupied density of states of the Pt 5d orbitals. An increase in the WL intensity indicates a decrease in the number of electrons (higher electron vacancy) in the Pt 5d orbitals. The significantly higher WL peak intensity demonstrated from Pt SAs and Pt SCs indicates that more 5d electron charge is depleted from the Pt sites; hence, higher unoccupied density of states of Pt 5d orbitals are obtained in the Pt SAs and Pt SCs compared with that of Pt NPs (Figure 3b). In addition, a positive shift in the threshold energy (E_0) can be observed for the Pt SAs and Pt SCs compared to Pt NPs and Pt foil (Figure 3c). The detailed E_0 value is determined from the normalized derivative spectra at the Pt L₃-edge. Specifically, the E_0 values for Pt SAs and Pt SCs are positively shifted to 11 565.3 and 11 565.2 eV, respectively, noticeably higher than that of 11 564.2 eV for Pt NPs and 11 564.0 eV for Pt foil. This shift is entirely consistent with the 5d charge depletion at the Pt site observed from the WL intensity increase, suggesting that Pt SAs and Pt SCs are losing more 5d electrons compared with that of Pt NPs. This is because the Pt atoms are connecting with the electronegative atoms such as N species from the ZIF-NC support, leading to the electron transfer from Pt SAs/SCs to the ZIF-NC support and thereby increases the 5d vacancy in the Pt site. The positive shift E_0 together with the significant increase in WL intensity indicates that Pt SAs and SCs are no longer in a metallic environment due to the isolated Pt atoms bonding with electron negative N/C species in ZIF-NC, while Pt NPs still maintain metallic character with strong Pt–Pt interactions. This discussion will be further confirmed by the later first-principles calculations.

Detailed information regarding the local bonding environment of Pt SAs, Pt SCs, and Pt NPs is obtained by fitting analysis of the Fourier transforms of the EXAFS data (Figure 3d), and corresponding structural parameters are shown in Table 1. In Figure 3d, there is a well-resolved metallic Pt–Pt contribution at 2.6 Å that can be detected in the sample of Pt NPs-ZIF-NC and Pt foil. By contrast, the Pt–N/C coordination at distance of 1.6 Å appears, and no Pt–Pt contribution at 2.6 Å (metallic bonding) or in the vicinity in the sample of Pt SAs-ZIF-NC can be detected, which well suggests the Pt atoms present in the isolated states. In addition to the predominant peak at 1.6 Å, a trace peak at 2.6 Å (Figure 3d; Figure S3b, Supporting Information) indicates the existence of Pt–Pt coordination for Pt SCs which is in agreement with the HAADF-STEM results. By theoretical modeling and fitting analyses of EXAFS data, the coordination numbers of Pt in Pt SAs, Pt SCs, and Pt NPs can be determined, and corresponding fitting model plots are

Table 1. EXAFS data fitting results of as-prepared ALDPt-ZIF-NC samples with Pt in SAs, SCs, and NPs.

Sample	Pt L ₃ E ₀ [eV]	Scattering path	Coordination number [N]	Radical distance [Å]	σ ² [Å ²]
Pt SAs-ZIF-NC	11 565.3	Pt–N/C	3.3	2.02	0.003
		Pt–Pt	0.176	2.774	0.0036
Pt SCs-ZIF-NC	11 565.2	Pt–N/C	3.027	2.02	0.0039
		Pt–Pt	0.819	2.774	0.0045
Pt NPs-ZIF-NC	11 564.2	Pt–Pt	6.05	2.774	0.0041
Pt foil	11 564.0	Pt–Pt	12	2.774	0.0045

E_0 : Position of the point of inflection of the rising edge; N: The coordination number for the absorber–back scatterer pair; R distance: The average absorber–backscatterer distance; and σ², the Debye–Waller factor.

shown in Figure S3 (Supporting Information). For the sample of Pt NPs-ZIF-NC, there is a Pt–Pt contribution at 2.6 Å (before phase correction) with an average coordination number of 6.02, which is lower than that of 12.0 in bulk Pt foil. As shown in Table 1, the coordination numbers of the Pt–Pt bonding in Pt SAs-ZIF-NC (0.176) and Pt SCs-ZIF-NC (0.819) are much lower than those in Pt NPs-ZIF-NC (6.05). The significantly lower Pt–Pt coordination number indicates the formation of Pt isolated atoms and subclusters instead of Pt crystals in Pt SAs-ZIF-NC and Pt SCs-ZIF-NC. Moreover, there is a prominent Pt–N/C contribution at a distance of 1.6 Å (before phase correction) in the radial distribution with average coordination numbers of 3.3 and 3.0 for Pt SAs and Pt SCs, respectively, suggesting the coordination model of Pt bonding with both N-dopants and carbon atoms, which show the direct evidence for the connecting and anchoring of N-doping sites to the Pt SAs. By combining HAADF-STEM and X-ray fine structure (XAFS) techniques, the SA, SC, and NP structures of Pt have been identified unequivocally. Subsequently, these catalysts with different Pt structures are tested for electrocatalysis toward the ORR.

The electrochemical performance of as-prepared ALDPt-ZIF-NC with Pt SAs, SCs, and NPs is evaluated in boosting the ORR. Cyclic voltammetry (CV) curves for the Pt SAs-ZIF-NC, Pt SCs-ZIF-NC, and Pt NPs-ZIF-NC are conducted in 0.1 M HClO₄ at a scanning rate of 50 mV s^{−1}. As the Pt loading is 0.8 wt% in Pt SAs-ZIF-NC and 1.5 wt% in Pt SCs-ZIF-NC, no obvious hydrogen adsorption/desorption peak is observed in the CV curves (Figure 4a). However, with increasing Pt loading to 10.5 wt%, the Pt NPs-ZIF-NC catalyst shows characteristic hydrogen adsorption/desorption peaks, suggesting crystalline Pt structures in the Pt NPs-ZIF-NC catalyst. The ORR activities of Pt SAs-ZIF-NC, Pt SCs-ZIF-NC, and Pt NPs-ZIF-NC are detected by conducting linear sweep voltammetry (LSV) on the catalyst-modified rotating disk electrode (RDE) in O₂-saturated 0.1 M HClO₄ under a rotating speed of 1600 rpm. Figure 4b shows that all the ALDPt-ZIF-NC catalysts with a Pt size from SAs to NPs can boost the ORR. In comparison with commercial 40%Pt/C, the Pt NPs-ZIF-NC catalyst shows better ORR performance with an obvious positive shift of the half-wave potential ($E_{1/2}$). It is shown that the $E_{1/2}$ values of 0.875 and 0.880 V (vs RHE) are demonstrated for Pt SAs-ZIF-NC and Pt SCs-ZIF-NC, respectively, which are lower than that of 0.895 V (vs RHE)

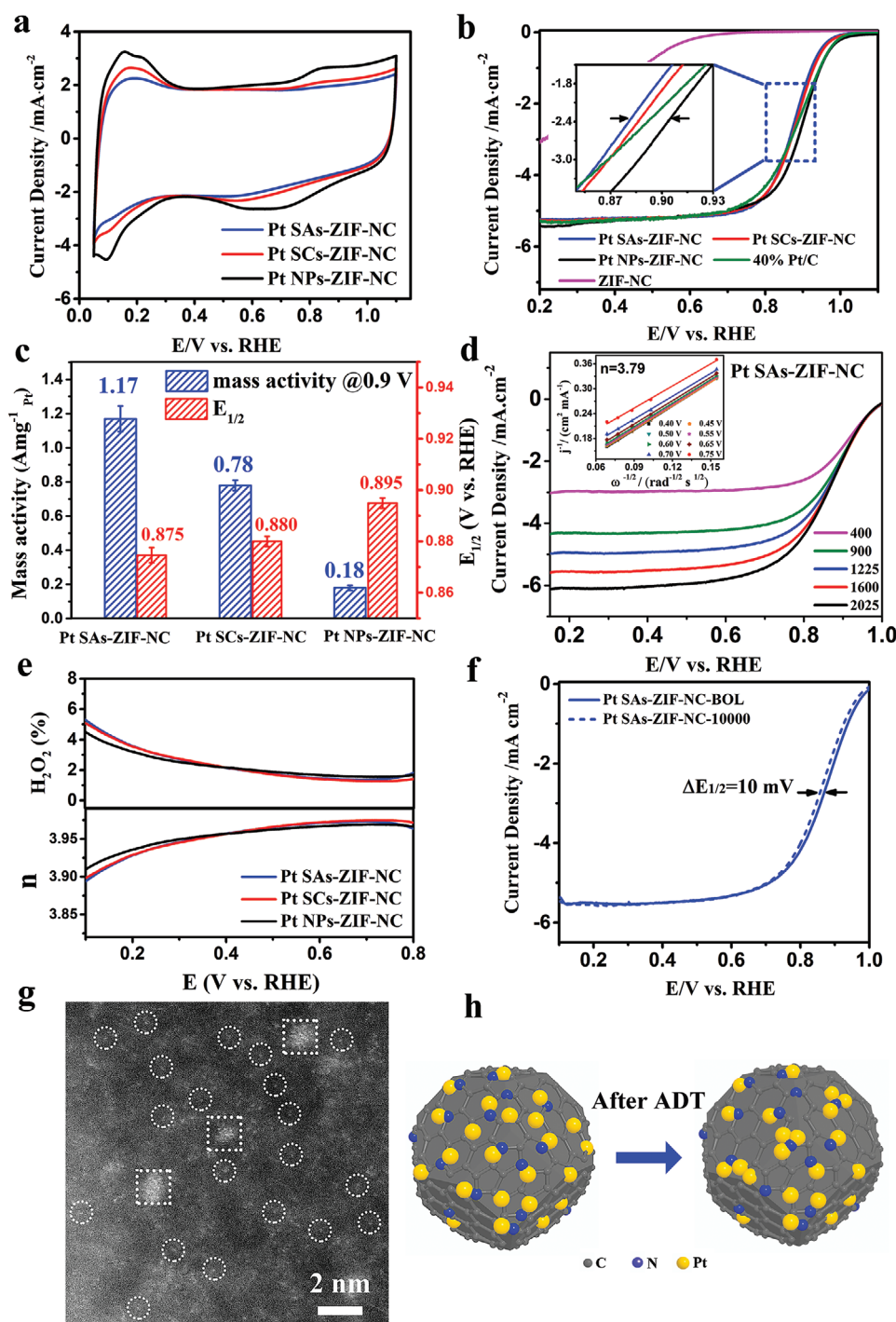


Figure 4. Electrocatalytic performance. a) The CV curves of ALD Pt-ZIF-NC samples in N_2 -saturated 0.1 M $HClO_4$ at a scan rate of 50 mV s^{-1} . b) The ORR polarization curves of ALD Pt-ZIF-NC samples in O_2 -saturated 0.1 M $HClO_4$ at a scan rate of 10 mV s^{-1} and a rotating speed of 1600 rpm. c) The normalized mass activity at 0.9 V (vs RHE) and the half-wave potential $E_{1/2}$ of the as-prepared ALD Pt-ZIF-NC catalysts. d) The ORR polarization curves of Pt SAs-ZIF-NC at different rotation speeds. Insets: Koutecky–Levich plots and electron transfer number. e) Electron transfer number (n) and H_2O_2 yield versus potential for as-prepared ALD Pt-ZIF-NC catalysts. f) The ORR polarization curves of Pt SAs-ZIF-NC before (BOL) and after 10 000 cycles potential cycling in O_2 -saturated 0.1 M $HClO_4$ at a scan rate of 10 mV s^{-1} and a rotating speed of 1600 rpm. g) The HAADF-STEM image and the h) schematic illustration for Pt SAs-ZIF-NC after 10 000 cycles' potential cycling test.

for Pt NPs-ZIF-NC (Figure 4c and Table 2). By analyzing the electrochemical-active surface area (ECSA) and specific activity of the ALD Pt-ZIF-NC catalysts, as indicated in Table 2, it was

found that the Pt SAs-ZIF-NC shows a specific activity of $0.51\text{ mA cm}^{-2}_{Pt}$ higher than that of $0.35\text{ mA cm}^{-2}_{Pt}$ for Pt SCs-ZIF-NC and $0.26\text{ mA cm}^{-2}_{Pt}$ for Pt NPs-ZIF-NC, implying the

Table 2. The parameters of catalyst loading, mass activity, specific activity, and electrochemical-active surface area (ECSA) of the as-prepared ALDPt-ZIF-NC samples toward the ORR.

Sample	Pt wt% in catalyst [wt%]	Catalyst loading on RDE [μg]	Pt loading on RDE [μg_{Pt}]	$E_{1/2}$ (vs RHE) [mV]	Kinetic current @0.9 V [mA cm^{-2}]	Mass activity @0.9 V [$\text{A mg}_{\text{Pt}}^{-1}$]	ECSA [$\text{m}^2 \text{g}^{-1}_{\text{Pt}}$]	Specific activity [$\text{mA cm}^{-2}_{\text{Pt}}$]
Pt SAs-ZIF-C	0.8	50	0.4	875 ± 3	2.39	1.17 ± 0.08	229	0.51
Pt SCs-ZIF-C	1.5	50	0.75	880 ± 2	2.97	0.78 ± 0.03	222	0.35
Pt NPs-ZIF-C	10.5	50	5.25	$895 \pm 2 \text{ mV}$	4.70	0.18 ± 0.02	66.7	0.26

enhanced electrochemical activity of Pt SAC toward the ORR. Furthermore, once normalized to Pt mass loading, the mass activity obtained through Koutecký–Levich equation^[13] for Pt SAs-ZIF-NC shows tremendous advancement. Remarkably, the high mass activity of $1.17 \text{ A mg}^{-1}_{\text{Pt}}$ is achieved for Pt SAs-ZIF-NC, which is 6.5 times greater than that of $0.18 \text{ A mg}^{-1}_{\text{Pt}}$ for Pt NPs-ZIF-NC catalyst (Figure 4c). The activity is better than those reported noble and transition metal SACs' activity toward ORR in the acidic media (Table S1, Supporting Information). The coordination of Pt SAs with N-doping sites leads to the electron transfer from Pt SAs to the ZIF-NC support and forms the Pt SAs with high electron vacancy in 5d orbitals, which results in the superior ORR activity and stability for the Pt SAs-ZIF-NC catalyst. To investigate the electron vacancy effect on electrochemical performance, the quantitative analysis of Pt L₃- and L₂-edge WL intensities of the XANES spectra is carried out (details are shown in the Supporting Information).^[7] The Pt L₃- and L₂-edge threshold (E_0), white line parameters, and the corresponding Pt 5d hole accounts (electron vacancy) of $h_{3/2}$ and $h_{5/2}$ are summarized in Table 3. The results show that Pt SAs exhibit total unoccupied densities of states of the 5d hole counts of 0.91, higher than that of 0.87 for Pt SCs and 0.79 for Pt NPs. The unsaturated coordination and high electron vacancy of Pt SAs suggest the electron transfer interaction between Pt SAs and the N-doped ZIF-NC support, which contributes to the tremendously enhanced electrocatalytic performance of Pt SAs. Moreover, the smaller size of Pt SAs enables them to offer more surface active sites at the constant Pt mass loading compared with Pt SCs and Pt NPs. High density of Pt SAs coordinated with rich N-sites on ZIF-NC provides sufficient active sites to boost the absorption/dissociation/reduction of O₂ molecules, thereby achieving a further enhanced mass activity of Pt SAC than Pt NP catalyst in promoting the ORR.

To gain insight into the reaction mechanism of Pt SAs-ZIF-NC, Pt SCs-ZIF-NC, and Pt NPs-ZIF-NC during ORR, RDE tests are performed at the different rotating speeds from 400 to 2025 rpm. Figure 4d shows that the current densities

are increased with increasing rotating speed, while the onset potential remains constant at different rotating speeds. Koutecký–Levich plots (Figure 4d, inset) show the good linearity and parallelism, indicating the first-order reaction kinetics of Pt SAs-ZIF-NC with regard to the oxygen concentration and a potential-independent electron transfer rate. The average electron transfer numbers of Pt SAs-ZIF-NC and Pt SCs-ZIF-NC are 3.79 (Figure 4d) and 3.81 (Figure S4a, Supporting Information), respectively, approaching that of Pt NPs-ZIF-NC ($n = 3.96$; Figure S4b, Supporting Information), implying a close four-electron oxygen reduction pathway for the ORR. The yields of H₂O₂ (%) for Pt SAs-ZIF-NC, Pt SCs-ZIF-NC, and Pt NPs-ZIF-NC are examined by rotating ring disk electrode (RRDE) measurements with a constant potential of 1.5 V (vs RHE) on the Pt ring. Less than 5% H₂O₂ yield was obtained for Pt SAs-ZIF-NC catalyst much similar to that of Pt SCs-ZIF-C and Pt NPs-ZIF-NC as shown in Figure 4e. The calculated electron transfer number through the H₂O₂ yield is around 3.9, further confirming an efficient four-electron ORR process occurred on the Pt SAs-ZIF-C catalyst in acid media.

Another challenge for the ultrasmall Pt SAC is their long-term stability in PEMFC application. The surface free energy of metal atoms increases with decreasing particle size, resulting in migration and aggregation occur and causing poor catalyst stability. An appropriate support with abundant anchoring sites that can strongly interact with the Pt atoms is favorable in fixing the finely dispersed Pt SAs. In this work, the long-time stability of ALDPt-ZIF-NC catalysts is evaluated by accelerated potential cycling of the electrode between 0.6 and 1.0 V (vs RHE) at 50 mV s^{-1} in O₂-saturated 0.1 M HClO₄ electrolyte. As exhibited in Figure 4f, the polarization curve of Pt SAs-ZIF-NC catalyst after 10 000 cycles accelerated durability test (ADT) maintained comparable onset potential and limiting current density with the beginning of life (BOL) performance, suggesting excellent durability performance during the ADT. Quantitatively, a 10 mV negative shift of $E_{1/2}$ is detected for Pt SAs-ZIF-NC

Table 3. Pt L₃-edge and Pt L₂-edge threshold and white line parameters of different catalysts.

Sample	Pt L ₃ edge WL				Pt L ₂ edge WL				Electron vacancy		
	E_0^{a} [eV]	$E_{\text{peak}}^{\text{b}}$ [eV]	Γ^{c} [eV]	ΔA_2^{d}	E_0^{a} [eV]	$E_{\text{peak}}^{\text{b}}$ [eV]	Γ^{c} [eV]	ΔA_2^{d}	$h_{5/2}$	$h_{3/2}$	Total
Pt foil	11 564	11 566.8	4.4	5.567	13 269.5	13 273.0	3.0	2.239	0.52	0.11	0.63
Pt SAs-ZIF-NC	11 564.8	11 567.7	7.0	7.726	13 273.9	13 273.4	5.6	4.356	0.71	0.20	0.91
Pt SCs-ZIF-NC	11 564.7	11 567.9	6.8	7.525	13 269.9	13 273.9	6.0	3.821	0.69	0.18	0.87
Pt NPs-ZIF-NC	11 564.4	11 567.1	6.4	6.888	13 269.5	13 273.1	5.8	3.200	0.64	0.15	0.79

^a)Position of the point of inflection of the rising edge; ^b)Peak position; ^c)Line width at half maximum of the WL; ^d)Area under the difference curve for unity edge jump; the unity edge jumps for the Pt L₃ and L₂ edges correspond to values of 2.5×10^3 and $1.16 \times 10^3 \text{ cm}^{-1}$, respectively.

and the mass activity (at 0.9 V vs RHE) decreased from 1.17 to 0.92 A mg⁻¹_{Pt} (with 21% loss of initial activity), which is still better than that of 0.73 and 0.12 A mg⁻¹_{Pt} revealed by Pt SCs-ZIF-NC and Pt NPs-ZIF-NC after 10 000 cycles' durability test (Figure S4c,d, Supporting Information). The high mass activity and comparable polarization curves of Pt SAs-ZIF-NC catalyst before and after ADT indicate the excellent activity and stability of the Pt SACs, which is attributed to the strong interactions between ALDPt SAs and the N-anchoring sites in ZIF-NC support.

Pt SAs-ZIF-NC and Pt NPs-ZIF-NC are further studied as cathode catalysts in membrane electrode assemblies (MEAs) for proton exchange membrane fuel cells. The open-circuit voltages of 0.950 and 0.946 V are achieved for Pt SAs-ZIF-NC- and Pt NPs-ZIF-NC-based MEAs, respectively, implying a comparable high intrinsic ORR activity of Pt SAs-ZIF-NC to that of commercial Pt/C catalyst in a single-cell application (Figure S5a, Supporting Information). Moreover, long-term durability tests were conducted using an ADT protocol suggested for PEMFCs by the U.S. Department of Energy (Experimental Section). Figure S5b-d (Supporting Information) shows the H₂-O₂ polarization curves for the single-cell MEA composed with Pt SAs-ZIF-NC, Pt NPs-ZIF-NC, and Pt/C cathode before and after the 5000 triangle potential cycles between 0.6 and 1.0 V at 50 mV s⁻¹. In case of Pt SAs-ZIF-NC-based MEA, 24 mV voltage loss at 0.8 mA cm⁻² was indicated after executing the ADT, while the Pt/C-based MEA showed a significant 36 mV performance loss after ADT due to the weak metal-support interaction, which suggests the excellent stability of Pt SAs-ZIF-NC under practical fuel cell operation. Based on the electrochemical results performed in both half-cell and single-cell systems, it is believed that Pt SAs-ZIF-NC catalyst shows excellent electrocatalytic activity and stability toward the ORR.

To discover the microstructure and size difference of Pt SAs after the ADT, the HAADF-STEM images of the post-testing Pt SAs-ZIF-NC catalyst are investigated. The HAADF-STEM image in Figure 4g indicates that most Pt species remain the isolated single atoms; only a few atoms are aggregated together and form the isolated clusters (≈1 nm size), and no crystalline Pt particles can be detected. The Pt SAs coordinated with N-doping sites show strong Pt SAs-support interactions that contribute to the high stability of Pt SAs-ZIF-NC catalyst during the long-time potential cycling. The other Pt atoms possessing weak interactions with the ZIF-NC support can easily move around and aggregate together to form Pt clusters (Figure 4h). Therefore, to further enhance the stability of Pt SACs, an ideal support with high density of anchoring sites is expected in the future. Based on the ALD nature and the N-rich ZIF-NC support, it is convincing that the strong interactions between Pt atoms and N-anchoring sites promise the Pt SAs-ZIF-NC with high ORR activity and good potential cycling stability.

To deeply understand the origin of electrocatalytic activity and stability of Pt SAs, first-principles calculations are applied to explore the electrochemical mechanism of the ORR for Pt SAs-ZIF-NC catalyst. The calculation results show that Pt SAs prefer to bond with the N-doping sites^[8] (Figure S6, Supporting Information); thereby N-dopants are discovered as the effective anchoring sites for Pt SAs. Based on the XAFS fact of

the 3.3 coordination number for Pt SAs, the proposed model of -Pt₁-N₁-C₂- is calculated to be the favorable structure in adsorption and anchoring of Pt SAs. In order to figure out efficient N species in anchoring Pt SAs, the ZIF-NC substrate with four different types of N species of pyridinic N, pyrrolic N, graphitic N, and oxidized N (based on the XPS analysis) is examined, and the results are shown in Figure S6 (Supporting Information). Comprehensive DFT computations of adsorption energies suggest that the adsorption of Pt atoms on ZIF-NC with pyridinic N is the most favorable site (see Figure S6 and Table S2 in the Supporting Information), which shows the much lower adsorption energies compared with other kinds of N species. Therefore, the ZIF-NC doped with pyridinic N sites is considered in the following calculations for understanding the ORR mechanism on Pt SAs-ZIF-NC catalyst.

The adsorption of oxygenated intermediates on Pt SAs-ZIF-NC is investigated to understand the ORR pathway. For comparison, the bulk Pt NPs composed with 44 atoms are also established. Initially, the O₂ molecule adsorption and reduction on the Pt SAs following mechanism I are considered. As shown in Figure 5a, O₂ is adsorbed on Pt SA-ZIF-NC in a side-on configuration. After a few step's reaction, the *O₂ is converted into *OH by reaction with proton-electron pairs, then *OH desorbs from the Pt SAs surface and releases Pt SA active sites to finish the ORR. The corresponding free energy diagrams for ORR are demonstrated in Figure 5b. It is found that the free energy (ΔG) of each procedure is downhill for the first few steps. However, the final step for *OH desorption, which is thermodynamically uphill (endothermic), indicating the desorption of *OH is the rate-determining step for ORR.^[14] The ΔG value for the final step of *OH desorption is up to +1.43 eV under the potential of 0.9 V, which means the poor catalytic activity under mechanism I.

Different from the bulk morphology, it is discovered that Pt SAs can adsorb more than one atom or species.^[8,15] Inspired by the difficulty in desorbing *OH from Pt SA as implied in mechanism I, the Pt SAs with one preadsorbed *OH is considered as the active site in boosting the ORR following pathway of mechanism II (Figure 5a). In the first step of mechanism II, an O₂ molecule adsorbs on the Pt SA with preadsorbed *OH can be converted into the intermediate of *OOH by reaction with a proton-electron pair (*OH + O₂ + (H⁺ + e⁻) to *OH + *OOH).^[16] Subsequently, the *OOH is further reduced by a proton-electron pair (H⁺ + e⁻) to generate the *O intermediate. During the reaction, the preadsorbed *OH does not directly get involved in the conversion reaction of O₂ into *OOH or *O intermediates, and it only acts as a spectator to affect the electronic structure of Pt SA. Notably, the following reactions in desorption the *O may occur through two different pathways (mechanisms II and III). One pathway is the desorption of *OH from PtSA*OOH (mechanism II); meanwhile, the *O combines with the proton-electron pair to produce another *OH on Pt SAs. The other way follows mechanism III, which reduces the *O into *OH and forms two *OH species on the Pt SAs-ZIF-NC sites. The corresponding free energy profiles for mechanisms II and III are shown in Figure 5b and Figure S7 (Supporting Information), respectively. At U = 0.9 V, both mechanisms II and III exhibit a relatively smaller ΔG for the rate-determining step than mechanism I. The ΔG = 0.17 eV for mechanism II is even smaller

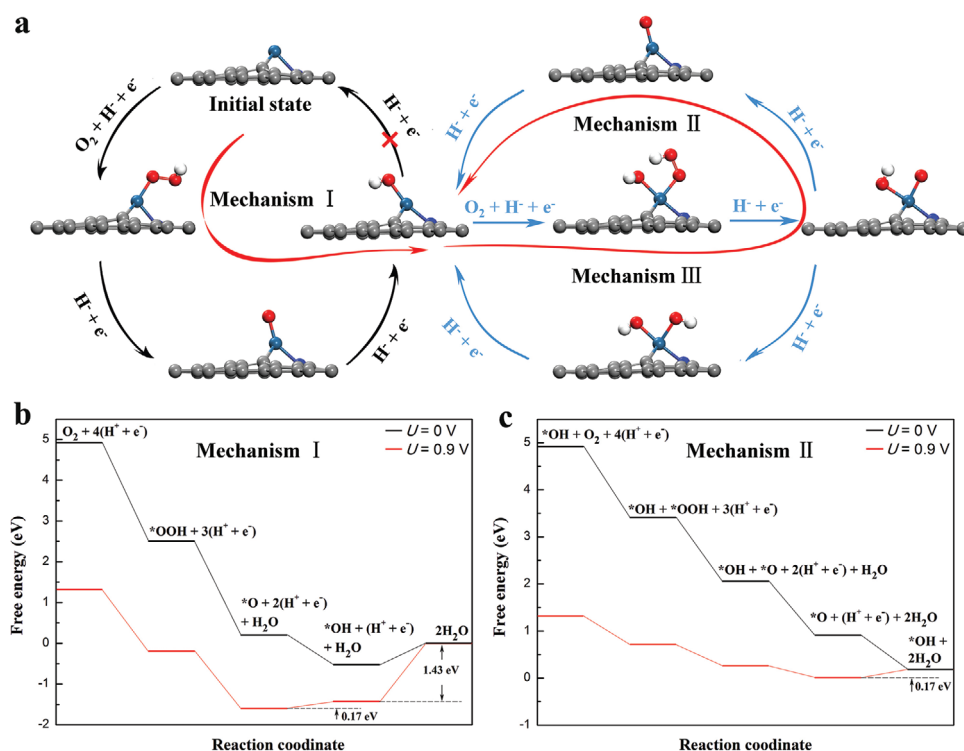


Figure 5. The reaction mechanism on the Pt SA and the corresponding free energy profiles. a) Three reaction mechanisms of ORR on Pt SAs-ZIF-NC. The first circle represents mechanism I. Both mechanism II (upper panel) and mechanism III (down panel) start from the intermediates stage with the OH adsorption on the Pt SA. The most favored pathway is highlighted with red arrows. b,c) The calculated free energy profiles of the ORR steps on Pt SAs-ZIF-NC based on mechanisms I and II. The black and red lines correspond to $U = 0$ and 0.9 V (vs RHE), respectively. U is the applied potential during the ORR. The gray, blue, green, red, and white balls represent the C, N, Pt, O, and H atoms, respectively.

than that of $\Delta G = 0.62$ eV need for mechanism III; thus, mechanism II should dominate over mechanism III in the ORR process on Pt SA with the preadsorbed *OH. Therefore, the ORR kinetic reaction mechanism on the Pt SAs-ZIF-NC first follows mechanism I to form the stable and active sites of Pt SA*OH through absorbing one O₂ molecule on the Pt SA. Subsequently, the oxygen reduction predominately triggered through the steps of mechanism II to gradually desorption of two *OH by overcoming a low free energy (0.17 eV). To fully understand the advantages of Pt SAs for the ORR, a typical Pt NP (Pt₄₄) constructed with 44 atoms is examined, and the calculated free energy profile of ORR steps on the Pt NP is shown in Figure S8 (Supporting Information). At $U = 0.9$ V, the free energy change for the last two steps of ORR on Pt NP becomes positive, and final step for *OH desorption (*OH + H⁺ + e⁻ → H₂O) is the rate-limiting step for the ORR on Pt NP, and the corresponding ΔG of the final step is the 0.26 eV. As discussed above, the Pt SAs have a lower ΔG value (0.17 eV) on the rate-determining step, which is smaller than that of Pt NPs (0.26 eV), indicating the better catalytic activity of Pt SAs than Pt NPs for the ORR.

As mentioned above, the Pt SA site with single *OH adsorption has much difficulty in desorption of *OH during the ORR. However, once co-adsorption of *OH with *O on Pt SA, the energy barrier for *OH desorption can be decreased and the catalytic activity of Pt SAs is significantly enhanced. In order to deeply understand why the co-adsorption of *O and *OH could tremendously improve the activity, the corresponding

density of states and oxide states of Pt SA are examined based on the occupation numbers^[17] and the unoccupied states. As the results shown in Figure 6 and Table S3 (Supporting Information), the initial d_{z²} orbitals of Pt SA are half-filled while d_{x²-y²} is empty. With single adsorption of *OH or *O, the p orbital of *OH mainly interacts with the d_{yz} orbital of Pt SA, resulting in the tilting toward d_{z²} (see Figure 6c). Interestingly, both d_{x²-y²} and d_{z²} become unoccupied for either *OH or *O adsorption. Then the d_{x²-y²} and d_{z²} of Pt SA are shifted to the high energy level, and the d_{x²-y²} stays at higher energy level. With further *OH adsorption on the *O adsorption configuration, *O shifts toward d_{xy} orbital, while the *OH prefers to stay along the direction of the d_{z²} instead of the d_{yz} as OH adsorption alone (see Figure 6c). It should be noted that d_{z²} is still unoccupied; meanwhile, d_{z²} is further pushed to a higher energy level than d_{x²-y²} (Figure 6a). Considering the rather high energy level of d_{z²}, the interaction between Pt and *OH in the situation of co-adsorption with *O should be much weaker than the one with *OH single adsorption. This should be the main reason why the *OH on the Pt-OOH is easier to desorb than that of pure Pt SA. Such results clearly indicate that the electronic structure of Pt SAs could be easily tuned to release *OH by the different adsorption style, which is the origin of the mechanism for the enhanced ORR activity revealed by the Pt SACs.

Moreover, the Bader charge population is also calculated to further reveal the stability of the Pt SAs. Owing to the

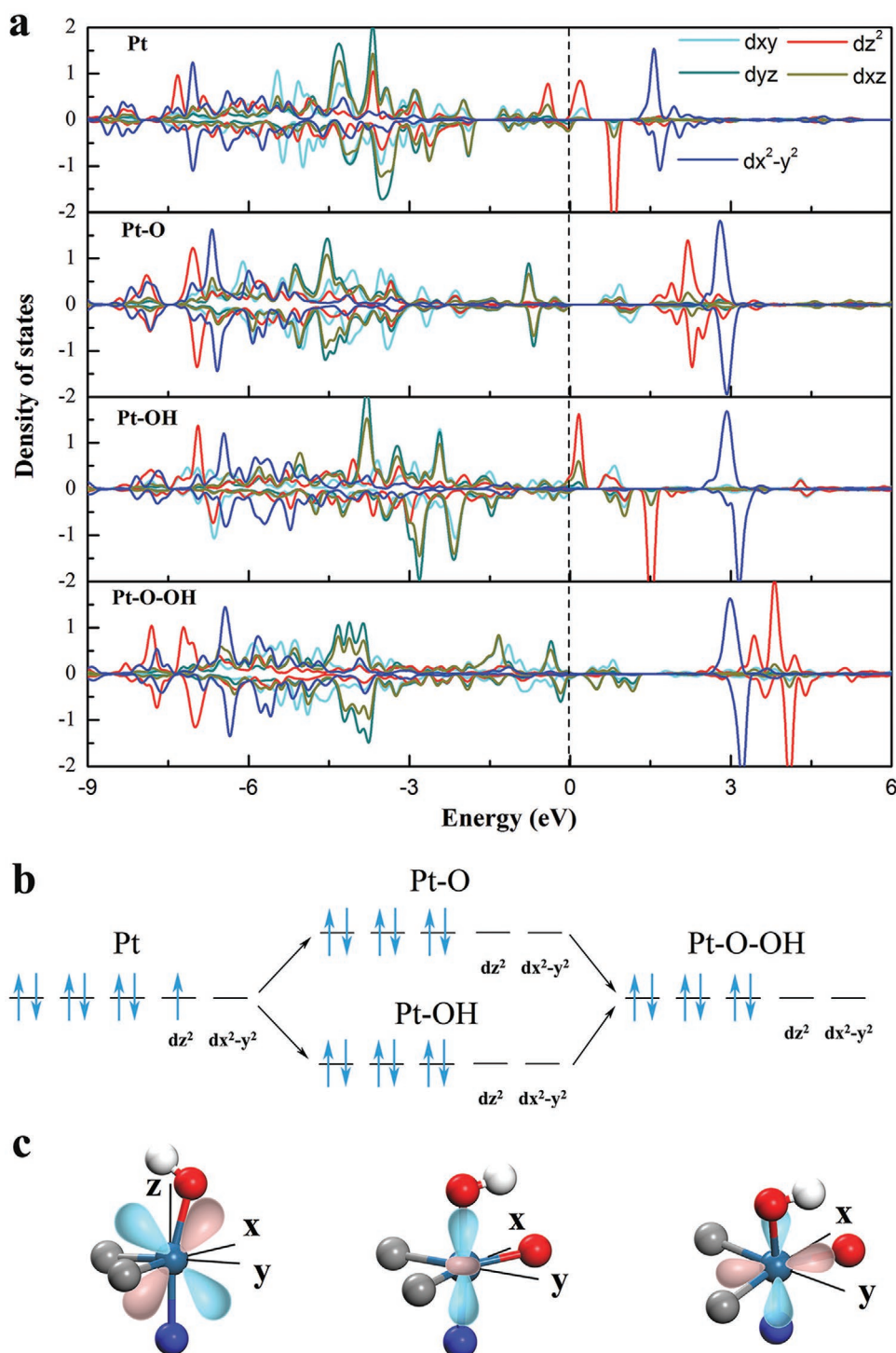


Figure 6. Schematic electronic structures of the Pt SAs with the different adsorptions. a) The calculated partially density of states (PDOSs) for the different kinds of adsorption on Pt SAs-ZIF-NC. Here, Pt, Pt-O, Pt-OH, and Pt-O-OH represent the clean, oxygen, hydroxyl, and co-adsorption of oxygen and hydroxyl, respectively. b) The d-orbital diagram for the different kinds of adsorptions derived from the occupied numbers (Table S3, Supporting Information). c) The three typical orbital interactions between Pt SA and the adsorptions: left— d_{yz} orbital for the *OH adsorption alone; middle and right— d_{z^2} and d_{xy} orbitals for the co-adsorption of *OH and *O, respectively. For simplicity, only the d orbitals are shown. The gray, blue, green, red, and white balls represent the C, N, Pt, O, and H atoms, respectively.

electronegativity between Pt SAs and N-dopants, there is charges transfer from Pt SAs to ZIF-NC. The DFT computations indicate that Pt SAs would transfer 0.28 and 0.38 more electrons

per Pt atom than Pt cluster and Pt NP to the ZIF-NC substrate, respectively (see Table S4 in the Supporting Information). The significant charge transfer suggests the strong interaction

between Pt SA with ZIF-NC substrate, which is well consistent with the XAFS analysis and the long-time electrochemical stability of Pt SAs. In all, DFT calculations further validate the excellent stability of Pt SA demonstrated from experimental results. It can be concluded that strong interactions between ALDPt SAs and the N-anchoring sites in ZIF-NC support contribute to the enhanced stability of Pt SACs.

3. Conclusion

In conclusion, a class of novel Pt catalysts from single atoms, subclusters, to nanoparticles supported by MOF-derived nanocarbon is proposed via the ALD technique. The HAADF-STEM and X-ray absorption fine spectra unequivocally identified the microstructure and local electronic environment of the Pt SAs, SCs, and NPs, which indicate that the isolated Pt single atoms tend to connect with the N-doping sites from the support. Subsequently, the catalysts with different Pt structures are tested for electrocatalysis toward the ORR. The Pt SAs-ZIF-NC catalyst shows superior stability performance and 6.5 times higher mass activity than Pt NP catalysts. Density functional theory calculations confirmed that Pt SAs prefer to be anchored by the pyridinic N sites from ZIF-NC support. Importantly, the Pt SAs exhibit versatile electronic structures with different adsorption species during the ORR. With co-adsorption of both hydroxyl and oxygen, the unoccupied orbitals of Pt SAs could be modulated with enhanced activity in the ORR. The ORR on Pt single-atom catalyst can occur in multichannel instead of single pathway as the Pt nanoparticle, which greatly decreases the free energy change for the rate-determining step and enhances the activity of Pt SAs for ORR. This work developed a promising approach in fabricating the single-atom catalyst and provided a deep understanding in the single-atom electrocatalysis for ORR, which holds great significance in preparing of low-cost and high-performing electrocatalysts for various reactions.

4. Experimental Section

See the details in the Supporting Information.

Supporting Information

Supporting Information is available from the Wiley Online Library or from the author.

Acknowledgements

Z.S., Y.-N.Z., and H.L. contributed equally to this work. This research was supported by Catalysis Research for Polymer Electrolyte Fuel Cells (CARPE-FC), Ballard Power Systems Inc., Natural Sciences and Engineering Research Council of Canada (NSERC), Canada Research Chair (CRC) Program, Canada Foundation for Innovation (CFI), Ontario Research Fund (ORF), Automotive Partnership of Canada, and the University of Western Ontario. The electron microscopy characterization was carried out at the Canadian Centre for Electron Microscopy (CEM), a national facility supported by NSERC, the Canada Foundation for Innovation (via the MSI program) and McMaster University. The X-ray

absorption spectra were performed at the Canadian Light Source which is supported by CFI, NSERC, CHIR, NRC, and the University of Saskatchewan. The author Z.S. was supported by the National Natural Science Foundation of China (Grant No. NSFC21905179). L.-M.L. was supported by the Science Challenge Project (TZ2018004), the National Natural Science Foundation of China (Grant Nos. 51861130360, 51572016, and U1930402), and Newton Advanced Fellowships under the grant No. NAF\R1\180242, the computation supports from Tianhe-2\JK computing time award at the Beijing Computational Science Research Centre (CSRC).

Conflict of Interest

The authors declare no conflict of interest.

Keywords

atomic layer deposition, density functional theory, metal-organic frameworks, oxygen reduction reaction, single-atom catalysts

Received: May 17, 2020

Revised: July 20, 2020

Published online:

- [1] a) M. K. Debe, *Nature* **2012**, *486*, 43; b) D. Banham, S. Ye, *ACS Energy Lett.* **2017**, *2*, 629; c) D. Banham, T. Kishimoto, Y. Zhou, T. Sato, K. Bai, J.-i. Ozaki, Y. Imashiro, S. Ye, *Sci. Adv.* **2018**, *4*, eaar7180; d) U. Eberle, B. Müller, R. von Helmolt, *Energy Environ. Sci.* **2012**, *5*, 8780.
- [2] a) D. Y. Chung, J. M. Yoo, Y.-E. Sung, *Adv. Mater.* **2018**, *30*, 1704123; b) R. F. Service, *Science* **2007**, *315*, 172; c) L. Su, W. Jia, C.-M. Li, Y. Lei, *ChemSusChem* **2014**, *7*, 361; d) S. Sui, X. Wang, X. Zhou, Y. Su, S. Riffat, C.-j. Liu, *J. Mater. Chem. A* **2017**, *5*, 1808; e) X. Cheng, Y. Li, L. Zheng, Y. Yan, Y. Zhang, G. Chen, S. Sun, J. Zhang, *Energy Environ. Sci.* **2017**, *10*, 2450; f) B. Genorio, R. Subbaraman, D. Strmcnik, D. Tripkovic, V. R. Stamenkovic, N. M. Markovic, *Angew. Chem., Int. Ed.* **2011**, *50*, 5468; g) Z. Song, B. Wang, N. Cheng, L. Yang, D. Banham, R. Li, S. Ye, X. Sun, *J. Mater. Chem. A* **2017**, *5*, 9760; h) Z. Song, M. N. Banis, L. Zhang, B. Wang, L. Yang, D. Banham, Y. Zhao, J. Liang, M. Zheng, R. Li, *Nano Energy* **2018**, *53*, 716.
- [3] Y.-J. Wang, N. Zhao, B. Fang, H. Li, X. T. Bi, H. Wang, *Chem. Rev.* **2015**, *115*, 3433.
- [4] a) J. Kim, H.-E. Kim, H. Lee, *ChemSusChem* **2018**, *11*, 104; b) X.-F. Yang, A. Wang, B. Qiao, J. Li, J. Liu, T. Zhang, *Acc. Chem. Res.* **2013**, *46*, 1740; c) N. Tian, B.-A. Lu, X.-D. Yang, R. Huang, Y.-X. Jiang, Z.-Y. Zhou, S.-G. Sun, *Electrochem. Energy Rev.* **2018**, *1*, 54; d) R. Wang, H. Wang, F. Luo, S. Liao, *Electrochem. Energy Rev.* **2018**, *1*, 324; e) L. Zhang, K. Doyle-Davis, X. Sun, *Energy Environ. Sci.* **2019**, *12*, 492; f) C. Zhu, S. Fu, Q. Shi, D. Du, Y. Lin, *Angew. Chem., Int. Ed.* **2017**, *56*, 13944; g) C. Wan, X. Duan, Y. Huang, *Adv. Energy Mater.* **2020**, *10*, 1903815.
- [5] a) H. Zhang, G. Liu, L. Shi, J. Ye, *Adv. Energy Mater.* **2018**, *8*, 1701343; b) J. Liu, M. Jiao, L. Lu, H. M. Barkholtz, Y. Li, Y. Wang, L. Jiang, Z. Wu, D.-j. Liu, L. Zhuang, C. Ma, J. Zeng, B. Zhang, D. Su, P. Song, W. Xing, W. Xu, Y. Wang, Z. Jiang, G. Sun, *Nat. Commun.* **2017**, *8*, 15938; c) X. X. Wang, D. A. Cullen, Y.-T. Pan, S. Hwang, M. Wang, Z. Feng, J. Wang, M. H. Engelhard, H. Zhang, Y. He, Y. Shao, D. Su, K. L. More, J. S. Spendelow, G. Wu, *Adv. Mater.* **2018**, *30*, 1706758; d) S. Yang, J. Kim, Y. J. Tak, A. Soon, H. Lee, *Angew. Chem., Int. Ed.* **2016**, *128*, 2098; e) H. Zhang,

- S. Hwang, M. Wang, Z. Feng, S. Karakalos, L. Luo, Z. Qiao, X. Xie, C. Wang, D. Su, Y. Shao, G. Wu, *J. Am. Chem. Soc.* **2017**, *139*, 14143; f) Y.-Q. Su, Y. Wang, J.-X. Liu, I. A. W. Filot, K. Alexopoulos, L. Zhang, V. Muravev, B. Zijlstra, D. G. Vlachos, E. J. M. Hensen, *ACS Catal.* **2019**, *9*, 3289; g) D. Zhao, Z. Zhuang, X. Cao, C. Zhang, Q. Peng, C. Chen, Y. Li, *Chem. Soc. Rev.* **2020**, *49*, 2215; h) M. Liu, L. Wang, K. Zhao, S. Shi, Q. Shao, L. Zhang, X. Sun, Y. Zhao, J. Zhang, *Energy Environ. Sci.* **2019**, *12*, 2890.
- [6] B. Qiao, A. Wang, X. Yang, L. F. Allard, Z. Jiang, Y. Cui, J. Liu, J. Li, T. Zhang, *Nat. Chem.* **2011**, *3*, 634.
- [7] S. Sun, G. Zhang, N. Gauquelin, N. Chen, J. Zhou, S. Yang, W. Chen, X. Meng, D. Geng, M. N. Banis, *Sci. Rep.* **2013**, *3*, 1775.
- [8] N. Cheng, S. Stambula, D. Wang, M. N. Banis, J. Liu, A. Riese, B. Xiao, R. Li, T.-K. Sham, L.-M. Liu, *Nat. Commun.* **2016**, *7*, 13638.
- [9] a) Z. Li, S. Ji, Y. Liu, X. Cao, S. Tian, Y. Chen, Z. Niu, Y. Li, *Chem. Rev.* **2020**, *120*, 623; b) S. Ji, Y. Chen, X. Wang, Z. Zhang, D. Wang, Y. Li, *Chem. Rev.* **2020**, <https://doi.org/10.1021/acs.chemrev.9b00818>; c) Y. Zhu, J. Sokolowski, X. Song, Y. He, Y. Mei, G. Wu, *Adv. Energy Mater.* **2020**, *10*, 1902844; d) Y. Wang, J. Mao, X. Meng, L. Yu, D. Deng, X. Bao, *Chem. Rev.* **2019**, *119*, 1806; e) Y. He, S. Liu, C. Priest, Q. Shi, G. Wu, *Chem. Soc. Rev.* **2020**, *49*, 3484.
- [10] a) Y. Chen, S. Ji, C. Chen, Q. Peng, D. Wang, Y. Li, *Joule* **2018**, *2*, 1242; b) A. Wang, J. Li, T. Zhang, *Nat. Rev. Chem.* **2018**, *2*, 65.
- [11] Y. He, Q. Tan, L. Lu, J. Sokolowski, G. Wu, *Electrochem. Energy Rev.* **2019**, *2*, 231.
- [12] a) X. Wang, W. Chen, L. Zhang, T. Yao, W. Liu, Y. Lin, H. Ju, J. Dong, L. Zheng, W. Yan, X. Zheng, Z. Li, X. Wang, J. Yang, D. He, Y. Wang, Z. Deng, Y. Wu, Y. Li, *J. Am. Chem. Soc.* **2017**, *139*, 9419; b) J. Li, M. Chen, D. A. Cullen, S. Hwang, M. Wang, B. Li, K. Liu, S. Karakalos, M. Lucero, H. Zhang, C. Lei, H. Xu, G. E. Sterbinsky, Z. Feng, D. Su, K. L. More, G. Wang, Z. Wang, G. Wu, *Nat. Catal.* **2018**, *1*, 935; c) Y. Chen, S. Ji, S. Zhao, W. Chen, J. Dong, W.-C. Cheong, R. Shen, X. Wen, L. Zheng, A. I. Rykov, S. Cai, H. Tang, Z. Zhuang, C. Chen, Q. Peng, D. Wang, Y. Li, *Nat. Commun.* **2018**, *9*, 5422; d) Z. Song, W. Liu, N. Cheng, M. N. Banis, X. Li, Q. Sun, B. Xiao, Y. Liu, A. Lushington, R. Li, L. Liu, X. Sun, *Mater. Horiz.* **2017**, *4*, 900; e) Y. Qu, Z. Li, W. Chen, Y. Lin, T. Yuan, Z. Yang, C. Zhao, J. Wang, C. Zhao, X. Wang, F. Zhou, Z. Zhuang, Y. Wu, Y. Li, *Nat. Catal.* **2018**, *1*, 781; f) C.-C. Hou, H.-F. Wang, C. Li, Q. Xu, *Energy Environ. Sci.* **2020**, *13*, 1658; g) C.-C. Hou, L. Zou, L. Sun, K. Zhang, Z. Liu, Y. Li, C. Li, R. Zou, J. Yu, Q. Xu, *Angew. Chem., Int. Ed.* **2020**, *59*, 7384; h) Y.-S. Wei, M. Zhang, R. Zou, Q. Xu, *Chem. Rev.* **2020**, <https://doi.org/10.1021/acs.chemrev.9b00757>.
- [13] K. Mayrhofer, D. Strmcnik, B. Blizanac, V. Stamenkovic, M. Arenz, N. Markovic, *Electrochim. Acta* **2008**, *53*, 3181.
- [14] a) J. Liu, M. Jiao, L. Lu, H. M. Barkholtz, Y. Li, Y. Wang, L. Jiang, Z. Wu, D.-j. Liu, L. Zhuang, *Nat. Commun.* **2017**, *8*, 15938; b) C. H. Choi, M. Kim, H. C. Kwon, S. J. Cho, S. Yun, H.-T. Kim, K. J. Mayrhofer, H. Kim, M. Choi, *Nat. Commun.* **2016**, *7*, 10922.
- [15] K. Huang, L. Zhang, T. Xu, H. Wei, R. Zhang, X. Zhang, B. Ge, M. Lei, J.-Y. Ma, L.-M. Liu, *Nat. Commun.* **2019**, *10*, 606.
- [16] J. K. Norskov, J. Rossmeisl, A. Logadottir, L. Lindqvist, J. R. Kitchin, T. Bligaard, H. Jonsson, *J. Phys. Chem. B* **2004**, *108*, 17886.
- [17] P. H.-L. Sit, R. Car, M. H. Cohen, A. Selloni, *Inorg. Chem.* **2011**, *50*, 10259.